Methane's solar radiative forcing

Byrom, R. E. and Shine, K. P. ORCID: https://orcid.org/0000-0003-2672-9978 (2022) Methane's solar radiative forcing. Geophysical Research Letters, 49 (15). e2022GL098270. ISSN 1944-8007 doi: 10.1029/2022GL098270 Available at https://centaur.reading.ac.uk/107079/

Geophysical Research Letters

RESEARCH LETTER
10.1029/2022GL098270

Methane's Solar Radiative Forcing

R. E. Byrom[1,2] **and K. P. Shine**[1]

[1]Department of Meteorology, University of Reading, Reading, UK, [2]Now at CICERO Center for International Climate Research, Oslo, Norway

Key Points:

- The net effect of solar radiative forcing by CH_4 is assessed with spatially and temporally resolved calculations
- CH_4 solar radiative forcing enhances CH_4 longwave-only radiative forcing by 7%
- This forcing is significantly sensitive to cloud radiative effect, CH_4 vertical profile, surface albedo and solar mid-infrared absorption

Supporting Information:

Supporting Information may be found in the online version of this article.

Correspondence to:

K. P. Shine,
k.p.shine@reading.ac.uk

Citation:

Byrom, R. E., & Shine, K. P. (2022). Methane's solar radiative forcing. *Geophysical Research Letters*, *49*, e2022GL098270. https://doi.org/10.1029/2022GL098270

Received 16 FEB 2022
Accepted 1 JUL 2022

Author Contributions:

Conceptualization: R. E. Byrom, K. P. Shine
Formal analysis: R. E. Byrom
Funding acquisition: K. P. Shine
Investigation: R. E. Byrom, K. P. Shine
Methodology: R. E. Byrom, K. P. Shine
Supervision: K. P. Shine
Visualization: R. E. Byrom
Writing – original draft: R. E. Byrom
Writing – review & editing: R. E. Byrom, K. P. Shine

Abstract Methane (CH_4) has significant absorption bands at wavelengths of 1.7, 2.3, 3.3 and 7.6 μm which absorb incoming solar 'shortwave' (SW) radiation and contribute to radiative forcing (RF). A comprehensive quantification of CH_4 SW RF is presented using a narrow-band radiative transfer model to calculate spatially and monthly resolved estimates of CH_4 SW RF and its impact on longwave (LW) stratospheric temperature adjusted RF (SARF). These new calculations include satellite measurements of CH_4 distribution and spectrally varying surface albedo, and include absorption of solar mid-infrared radiation by methane's 7.6 μm band. These factors substantially influence methane's SW effect. For a 750–1,800 ppb perturbation, the all-sky top-of-atmosphere SW instantaneous RF is 0.082 W m^{-2}; at the tropopause it is 0.002 W m^{-2}, considerably smaller than previous estimates. Including the impact of SW absorption on stratospheric temperature increases tropopause SARF by 0.039 W m^{-2} (or 7%) compared to the LW-only SARF.

Plain Language Summary Radiative forcing is a widely used metric to quantitatively compare the strength of different drivers of climate change. It measures the perturbation to Earth's energy balance, such as that due to an increase in greenhouse gas concentrations. Most greenhouse gas forcings arise due to absorption of thermal infrared ("longwave") radiation, but greenhouse gases also absorb solar radiation. However, methane's solar radiative forcing has received relatively little attention. We present the most detailed calculation of methane's solar radiative forcing to date, when concentrations increase from pre-industrial to present day levels (750–1,800 parts per billion). Our calculations exploit recent satellite measurements and we also quantify the effect of absorption of solar radiation at mid-infrared wavelengths. These factors substantially influence methane's SW effect. At the top-of-atmosphere, methane's all-sky solar radiative forcing is 0.082 W m^{-2}; at the tropopause it is 0.002 W m^{-2}, considerably smaller than previous estimates. However, methane's absorption of solar radiation heats the stratosphere; this heating significantly modifies methane's longwave radiative forcing. When this effect is included we find that methane's absorption of solar radiation enhances methane's longwave radiative forcing by 0.039 W m^{-2} (or 7%) from 0.574 W m^{-2} to 0.613 W m^{-2}.

1. Introduction

CH_4 is the second largest contributor to greenhouse gas radiative forcing (RF; Forster et al., 2021). It predominantly interacts with thermal-infrared longwave (LW) irradiances, but also absorbs incoming solar shortwave (SW) radiation, mainly at near-infrared (NIR) wavelengths (0.7–4 μm). CH_4 SW absorption is not explicitly treated in radiative transfer codes in all Earth System Models (ESMs) (e.g., Smith et al., 2018) and its radiative effect has been relatively unexplored.

Several RF definitions are available, each progressively better at characterizing surface temperature impact (Forster et al., 2021; Myhre, Shindell, et al., 2013). Instantaneous RF (IRF) results from a change in target constituent only, most often diagnosed at the tropopause or top-of-atmosphere (TOA) (Ramaswamy et al., 2019). SARF incorporates rapid stratospheric temperature adjustments resulting from heating rate perturbations due to the target constituent change; it is identical at tropopause and TOA. Effective Radiative Forcing (ERF) incorporates additional atmospheric rapid adjustments (calculated using an ESM) that occur independently of surface temperature change; it is normally presented at TOA.

Few recent studies have explored the significance of CH_4 SW RF. Etminan et al. (2016) presented calculations using the Oslo line-by-line (LBL) code (see Myhre et al., 2006) for two atmospheric profiles (tropical/extratropical) to estimate global-mean tropopause CH_4 SW IRF and its effect on LW SARF. They demonstrated two key components of CH_4 SW RF. Firstly, CH_4 SW absorption bands exert a positive all-sky tropopause IRF of 0.03 W m^{-2} following a 750–1,800 ppb perturbation. Secondly, the subsequent stratospheric heating enhances

the magnitude of CH_4 SARF. Consequently, they reported a 15% increase in 1750–2011 CH_4 SARF relative to the Intergovernmental Panel on Climate Change (IPCC) Fifth Assessment Report (Myhre, Shindell, et al., 2013) value. This revision underscored the importance of incorporating CH_4 SW absorption in RF calculations and emission metrics. They estimated a ±25% uncertainty due to a range of factors including: specification of surface albedo (α_s), computation of day-averaged forcings and their simple method of spatial and temporal averaging. Collins et al. (2018) later presented spatially resolved calculations of CH_4 SW tropopause IRF using a narrow-band radiative transfer code and background climatologies from two ESMs. For an 806–1,760 ppb perturbation, they reported global annual-mean all-sky CH_4 SW tropopause IRFs of ≈0.026 W m^{-2} and demonstrated that its distribution depended significantly on NIR α_s. Collins et al. (2018) did not quantify the effect of SW absorption on SARF.

This letter presents the most detailed quantification of the CH_4 SW effect to date. A narrow-band radiative transfer model is used to calculate seasonally and spatially resolved forcings (Section 2). These calculations utilize satellite measurements of CH_4 and spectrally resolved α_s to derive a best estimate of global annual-mean CH_4 SW IRF and LW and net SARF (Section 3). Comparisons with Etminan et al. (2016) and Collins et al. (2018) highlight key sensitivities, namely the effect of CH_4 SW absorption at solar mid-infrared wavelengths, the vertical representation of CH_4 mole fraction and the specification of spectrally resolved α_s. To compare with previous studies, we initially focus on tropopause SW IRF. We then calculate SARF and demonstrate the usefulness of diagnosing SW IRF at the TOA in line with the ERF concept. The use of SARF allows higher spectral resolution radiation calculations than are practicable in ESMs; this is especially important as there are indications that lower resolution ESM radiation codes underestimate CH_4 SW RF (Section 4).

2. Models, Methods and Data

RF calculations use the two-stream radiative transfer model, SOCRATES-RF (Checa-Garcia et al., 2018), which utilizes the radiance core of the UK Met Office Suite Of Community RAdiative Transfer codes based on Edwards and Slingo (SOCRATES, Edwards & Slingo, 1996; Manners et al., 2015) to compute IRF and SARF using the fixed dynamical heating (FDH) approximation (e.g., Fels et al., 1980) which allows a first-order estimate of stratospheric temperature change.

SW IRFs are calculated using a 260-band spectral file (sp_sw_260_jm2) covering wavelengths from 0.17 to 10 μm. This file has been verified against LBL codes for a variety of scenarios by Walters et al. (2019); it is independently validated here against the LBL Reference Forward Model (RFM) (see Dudhia, 2017), exhibiting a mean error of 8% across a range of conditions. sp_sw_260_jm2 uses solar spectral data from the Naval Research Laboratory Solar Spectral Irradiance model (Lean et al., 2005) averaged across 2000–2011. Gaseous absorption uses the correlated-k distribution method based on HITRAN2012 spectroscopic data (Rothman et al., 2013). SW gaseous overlap is treated using the 'equivalent extinction with correlated scaling' method, as recommended for computational efficiency (Manners et al., 2015). LW forcings use the standard broadband spectral file configuration (sp_lw_ga7) with nine bands across 3.34–10,000 μm (Walters et al., 2019). This lower resolution configuration was used due to the computational expense of performing spatially and seasonally resolved FDH calculations. In comparison to the 300-band LW spectral file (sp_lw_300_jm2), January all-sky LW IRF differs by less than 2% when gaseous absorption is treated using the more accurate 'random overlap' assumption. Hence this method of treating gaseous overlap is used for LW calculations here.

H_2O continuum absorption is based on MT_CKD 2.5 (Mlawer et al., 2012) with modifications in some NIR window regions using experimental data (Ptashnik et al., 2011, 2012). Calculations are conducted under clear-sky and all-sky conditions. Temperature, humidity and cloud fields are taken from ERA-interim reanalysis (Dee et al., 2011). Vertical cloud overlap is treated assuming random overlap. Whilst this does not account for cloud inhomogeneity and 3D effects, cloud optical parameters are characterized with high spectral resolution across 260-bands in sp_sw_260_jm2, with ice and water clouds treated separately within three atmospheric layers. Aerosols are absent from calculations.

CH_4 mole fractions are derived from the Michelson Interferometer for Passive Atmospheric Sounding (MIPAS) climatology (Hegglin et al., 2021), comprising zonal-mean values averaged between 2005 and 2012 from 300 hPa to 0.1 hPa at a 5° spatial resolution. Text S2 in Supporting Information S1 describes this dataset further and details how these fields are utilized to construct pre-industrial CH_4 mole fraction profiles. Briefly, at each latitude

Table 1
Global Annual-Mean Clear-Sky and All-Sky SW, LW and Net IRF at TOA, Tropopause and Surface Following a 750–1,800 ppb CH_4 Perturbation

	Clear-sky IRF (W m^{-2})			All-sky IRF (W m^{-2})		
	SW	LW	Net	SW	LW	Net
TOA	0.040	0.650	0.690	0.082	0.553	0.635
Tropopause	−0.038	0.674	0.636	0.002	0.578	0.580
Surface	−0.235	0.306	0.071	−0.163	0.180	0.017

Note. Derived using MIPAS CH_4 fields and SCIAMACHY-SSA α_s. LW, longwave; SW, shortwave.

profiles are constructed using the fall-off rate of MIPAS CH_4 with a value of 750 ppb at 300 hPa. This results in well-mixed tropospheric CH_4 and latitudinally dependent, vertically varying CH_4 at pressures below 300 hPa (Figure S3 in Supporting Information S1). The perturbed CH_4 SOCRATES-RF simulation uses the same fall-off rate but with mole fractions scaled to 1,800 ppb at 300 hPa.

α_s is derived from 33 one-nm wavelength bands between 0.355 and 2.314 μm from the Scanning Imaging Absorption spectroMeter for Atmospheric CHartograhY (SCIAMACHY) Lambertian-equivalent reflectivity (LER) database (version 2.6; Tilstra et al., 2017) averaged between 2002 and 2012 at 0.5° × 0.5° spatial resolution. LER is defined as the reflectance of an isotropic surface required to match observed TOA reflectance in a clear-sky, aerosol-free Rayleigh scattering atmosphere (e.g., Kleipool et al., 2008). This dataset implicitly includes the effect of spatial and temporal variation in snow cover and sea-ice on spectral α_s (see Text S3 in Supporting Information S1). Given the lack of alternative observationally based, spectrally resolved global α_s datasets at $0.355 > \lambda > 2.314$ μm, this approach constructs a best estimate of spectral surface reflectance across 0.17–10 μm. LER data exhibit unrealistically low NIR α_s (≈0.001–0.008) over sea-surfaces; therefore these data points have been replaced with spectrally varying α_s calculated using a SOCRATES internal subroutine (see Text S3 in Supporting Information S1). Consequently, α_s fields amalgamate SCIAMACHY and SOCRATES sea-surface α_s (henceforth referred to as SCIAMACHY-SSA) re-gridded to a 5° × 5° spatial resolution.

SOCRATES-RF adopts a tropopause pressure based on the parametric equation of Checa-Garcia et al. (2018) which describes a hemispherically symmetric tropopause (see Equation S1 in Supporting Information S1). This prescribes annual-mean tropopause height following the climatological tropopause representation by Hansen et al. (2005). SARF calculations require this tropopause pressure, as stratospheric temperatures are only adjusted at pressures lower than this. A six-point Gaussian quadrature method is used to calculate the diurnal variation of solar radiation. All calculations are performed using monthly mean input fields except for sensitivity tests in Section 3.2 where forcings are calculated using the four mid-season months (January, April, July, and October). The average of these months (referred to as quasi-annual mean) differs from the full-annual all-sky SW IRF by less than 1% at the TOA, tropopause and surface for a doubling of CH_4.

3. Radiative Forcing Calculations

3.1. Clear-Sky and All-Sky CH_4 SW IRF

Table 1 shows global annual-mean SW IRF at the TOA, tropopause and surface for a CH_4 perturbation from 750 to 1,800 ppb, the approximate pre-industrial and present-day values used in Etminan et al. (2016). Corresponding LW and net IRFs are also shown to demonstrate the impact of SW absorption on total IRF.

For clear-skies, SW IRF is positive at TOA (0.040 W m^{-2}) driven by enhanced absorption of surface-reflected radiation between the surface and TOA. At the tropopause and surface, SW IRF is negative due to a reduction in downward SW irradiance with enhanced CH_4 absorption in the stratosphere and troposphere. The surface SW IRF of −0.235 W m^{-2} counterbalances the surface LW IRF of 0.306 W m^{-2}, giving a net forcing of 0.071 W m^{-2}. Under all-sky conditions this offset is enhanced resulting in a net forcing of just 0.017 W m^{-2}. This demonstrates the importance of CH_4 SW absorption on surface energy budgets.

The all-sky TOA SW IRF increases from the clear-sky value of 0.040 W m^{-2} to 0.082 W m^{-2} due to absorption of increased reflected SW radiation by cloud radiative effect (CRE). This mechanism is also responsible for the switch in sign of the tropopause SW IRF from −0.038 W m^{-2} to 0.002 W m^{-2}. This all-sky tropopause SW IRF is significantly smaller than Etminan et al. (2016) and Collins et al. (2018) (0.03 and ≈ 0.026 W m^{-2}, respectively). Section 3.1.1 and Section 3.2 address this disparity.

Figure 1 shows the spatial distribution of annual-mean all-sky SW tropopause IRF (upper left) and the corresponding CRE (lower left). The distribution of SW IRF is comparable to Collins et al. (2018) exhibiting regions of maxima over the Arabian Peninsula and the Sahara (exceeding 0.20 W m^{-2}). Strong spatial gradients in the

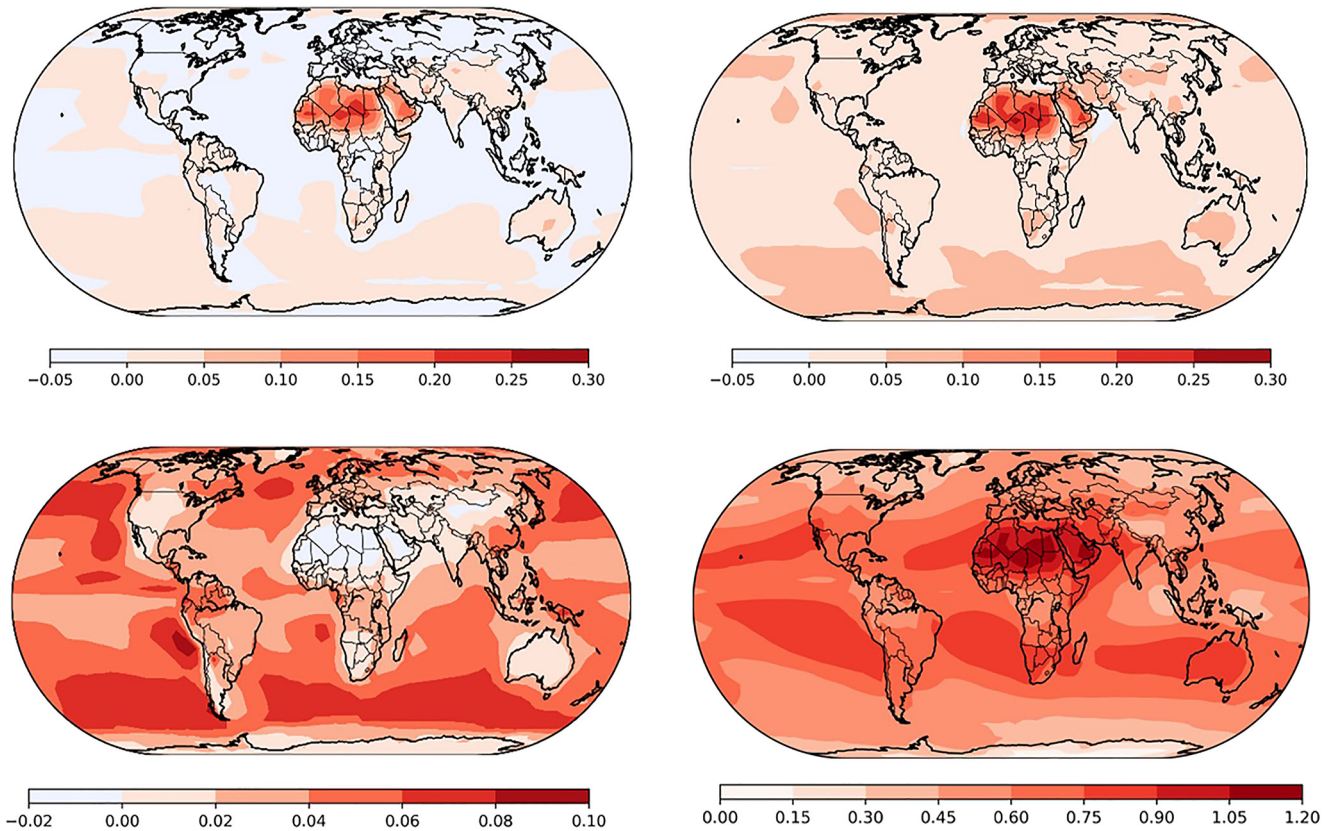

Figure 1. All annual-mean (W m^{-2}). Upper left: All-sky tropopause SW IRF. Lower left: Cloud radiative effect on tropopause SW IRF calculated as the difference between all-sky and clear-sky conditions. Upper right: Total all-sky SW RF at the tropopause derived as the difference between net SARF (i.e., LW SARF (including SW in FDH calculation) + SW IRF) and LW-only SARF. Lower right: All-sky net SARF at the tropopause. Derived using conditions stated in Table 1 note. Global-mean forcings are given in Table 2.

forcing are driven by spectrally resolved NIR α_s for desert surfaces. As explained by Collins et al. (2018), such surfaces increase the reflection of downwelling SW irradiance, enhancing the magnitude of tropospheric CH_4 SW absorption causing a more positive IRF. CRE is predominantly positive with a localized maximum of 0.1 W m^{-2} off the west coast of South America associated with oceanic stratocumulus cloud decks. Regions with negative CRE dampen the influence of α_s on IRF magnitude, particularly across northern Africa due to high NIR α_s of desert surfaces.

3.1.1. Comparison With Previous Studies

Etminan et al. (2016) were the first to highlight the importance of CRE in determining the sign and magnitude of tropopause SW IRF; CRE increased their clear-sky SW tropopause IRF of −0.045 W m^{-2} by 0.075 W m^{-2} to an all-sky value of 0.03 W m^{-2}. The results presented here confirm the importance of CRE, albeit with a less pronounced increase (0.04 W m^{-2}).

By contrast, Collins et al. (2018) calculate positive (rather than negative) clear-sky tropopause SW IRFs of 0.0095 W m^{-2} (the average of their two ESM climatologies). They attribute this to the use of realistic surface conditions in their spatially resolved simulations; this cannot be the full explanation as it disagrees with the spatially resolved simulations with spectrally varying α_s presented here. CRE enhances their IRF by an average of 0.016 W m^{-2}, much less than the present results and Etminan et al. (2016). Although the Collins et al. (2018) global-mean all-sky SW tropopause IRF of approximately 0.026 W m^{-2}, is similar to the Etminan et al. (2016) estimate of 0.03 W m^{-2}, disagreement in the sign of clear-sky IRF and the size of CRE indicates that this agreement is coincidental.

3.2. Sensitivities of CH_4 SW Radiative Forcing

The all-sky SW tropopause IRF of 0.002 W m^{-2} is significantly smaller than Etminan et al. (2016) and Collins et al. (2018) due to a combination of factors that alter the relative importance of downward and upward tropopause forcing components. As explained by Etminan et al. (2016) (see also Shine et al., 2022), the tropopause SW IRF is a residual of reduced downward irradiance (due to absorption in the stratosphere, which constitutes a negative IRF) and reduced upward irradiance (due to absorption of surface-troposphere reflected irradiance in the troposphere, which constitutes a positive IRF). The following sub-sections detail these factors using a range of sensitivity tests, which are also likely relevant to the calculation of SW RF of other gases.

3.2.1. The Representation of CH_4 Vertical Profiles

CH_4 decreases with height above the tropopause due to chemical destruction. A realistic vertical distribution is necessary because stratospheric SW absorption contributes significantly to the sign and magnitude of all-sky SW tropopause IRF (Figure S7 in Supporting Information S1).

Sensitivity tests demonstrate the need for a realistic description of the spatial and temporal variability in stratospheric CH_4. SOCRATES-RF experiments were repeated using Section 2 methodology, but with idealized zonal-mean CH_4 mole fraction scale-heights from the CAM3.0 model (Collins et al., 2004), as used by Collins et al. (2018) (based on early 2-dimensional chemical model simulations—see Text S4 in Supporting Information S1). These do not represent hemispherical and seasonal differences in stratospheric CH_4. Unlike CAM3.0's smooth exponential decrease, 'MIPAS' has more CH_4 in the stratosphere and its mole fractions vary monthly with a variable rate of decrease with height at each latitude (see Figures S5 and S6 in Supporting Information S1). At 3 hPa, MIPAS values are at least 2.5 times larger than CAM3.0 values at 0° and over 10 times larger at 60° and 90°N/S.

'CAM3.0' scale-heights give an all-sky SW tropopause IRF of 0.009 W m^{-2} whereas MIPAS mole fractions give an IRF of 0.002 W m^{-2} (Table 1). This difference originates from the size of the downward SW forcing component. MIPAS values increase stratospheric CH_4 SW absorption at both pre-industrial and present-day levels, causing a more negative downward IRF at the tropopause. Hence, the positive upward forcing component (due to CRE) makes the MIPAS forcing only weakly positive, but decisively positive for CAM3.0.

3.2.2. Impact of CH_4 Absorption Between 5 and 10 μm

Solar spectral irradiance extends beyond the NIR; around 5.4 W m^{-2} occurs in the 5–10 μm region. Although only about 0.5% of total solar irradiance, this spectral region contains the strong 7.6 μm CH_4 absorption band (primarily responsible for CH_4 LW RF) (Li et al., 2010). In exploratory calculations using CAM3.0 CH_4 profiles and spectrally constant α_s fields from ERA-interim reanalysis data (Dee et al., 2011), the 5–10 μm all-sky CH_4 SW tropopause IRF is found to be −0.004 W m^{-2} compared to the 0.17–10 μm value of 0.016 W m^{-2}. The negative forcing demonstrates that this spectral region mainly impacts stratospheric absorption. Neglecting this contribution would overestimate the all-sky SW tropopause IRF by 25%, for this configuration; hence the 5–10 μm region is included in calculations presented here. Both Etminan et al. (2016) and Collins et al. (2018) use an upper wavelength limit of 5 μm. The spectral nature of CH_4 SW IRF was considered in detail in Etminan et al. (2016); Figure S7 in Supporting Information S1 extends this to include methane's 7.6 μm band.

3.2.3. Sensitivity to Spectrally Varying Albedo

The spatial and spectral variation in α_s depends on factors including surface type, season and solar zenith angle. SOCRATES-RF experiments demonstrate the importance of spectrally varying α_s in controlling the amount of surface-reflected SW radiation absorbed by CH_4. The use of spectrally constant ERA-interim α_s in forcing calculations overestimates the reflected SW radiation absorbed by CH_4 predominantly in polar regions, yielding a global-mean all-sky SW tropopause IRF of 0.016 W m^{-2} compared to 0.009 W m^{-2} using SCIAMACHY-SSA α_s (both calculated using SOCRATES-RF with CAM3.0 CH_4; see Figure S8 in Supporting Information S1).

Both Etminan et al. (2016) and Collins et al. (2018) incorporate spectrally varying α_s. Etminan et al. (2016) use broadband values taken from OsloCTM2 simulations (Myhre, Samset, et al., 2013). Collins et al. (2018) use land and snow α_s "obtained from climate model grid spectral seven-band Moderate Resolution Imaging Spectroradiometer bi-directional reflectance distribution functions" covering the 0.620–2.155 μm wavelength range. Here, the use of SCIAMACHY α_s data (with 33 bands across 0.355–2.314 μm) provides a more spectrally

Table 2
Global Annual-Mean All-Sky TOA, Tropopause and Surface SW IRF, LW SARF (Including SW Heating Rates in the FDH Calculation), Net SARF (SW IRF + LW SARF) and LW-Only SARF (Excluding SW Heating Rates in the FDH Calculation)

	All-sky CH_4 RF (W m^{-2})			
	SW IRF	LW SARF	Net SARF	LW-only SARF
TOA	0.082	0.530	0.613	0.574
Tropopause	0.002	0.611	0.613	0.574
Surface	−0.163	0.181	0.018	0.179

Note. Derived using conditions stated in Table 1 note. LW, longwave; SW, shortwave.

resolved description of land and sea-ice α_s. The representation of ocean α_s here (Section 2) and in Collins et al. (2018) is of similar complexity, based on Cox and Munk (1954).

Summarizing, the combined effect of the above sensitivities results in a significantly smaller all-sky CH_4 SW tropopause IRF compared to earlier estimates. MIPAS fields significantly improve the representation of the spatial and temporal variation in stratospheric CH_4, SCIAMACHY-SSA provides a more highly spectrally resolved description of α_s and SOCRATES includes solar CH_4 absorption between 5 and 10 μm.

3.3. Radiative Forcing Including Stratospheric Temperature Adjustment

The total SW effect is quantified by comparing the net SARF, calculated due to both SW and LW absorption, with the SARF calculated due to LW absorption alone. Table 2 shows all-sky SW IRF, LW SARF (where SW absorption is *included* in the FDH calculation), net SARF (SW IRF plus LW SARF) and LW-only SARF (where SW absorption is *excluded* from the FDH calculation). The SW forcing is only minimally affected by the temperature change; hence SW IRF and SW SARF are identical.

The tropopause SW IRF of 0.002 W m^{-2} is only a small fraction (0.3%) of net SARF (0.613 W m^{-2}). However, when SW absorption is included in the calculation of stratospheric temperature adjustment, net SARF increases by 7% to 0.613 W m^{-2} from the LW-only SARF of 0.574 W m^{-2}. This difference of 0.039 W m^{-2} is 20 times larger than the tropopause SW IRF itself, emphasizing that the contribution of SW absorption to net SARF should not be assessed by considering the impact on SW fluxes alone.

Figure 2 compares the stratospheric temperature difference (ΔT) calculated using FDH for LW-only and LW plus SW heating rates. In the LW-only case (left panel), increased CH_4 leads to a cooling across most of the stratosphere, exceeding 0.2 K in the upper stratosphere. A small warming is evident above the tropical tropopause; however, this does not counterbalance the impact of the cooling on downward LW irradiance at the tropopause, which slightly decreases the LW forcing from 0.578 W m^{-2} (Table 1) to 0.574 W m^{-2} (Table 2). When SW absorption is included (right panel), the cooling is reduced across the entire stratosphere and reverses sign in the lower stratosphere, giving a strong warming reaching a maximum ΔT of 0.5 K above the tropical tropopause.

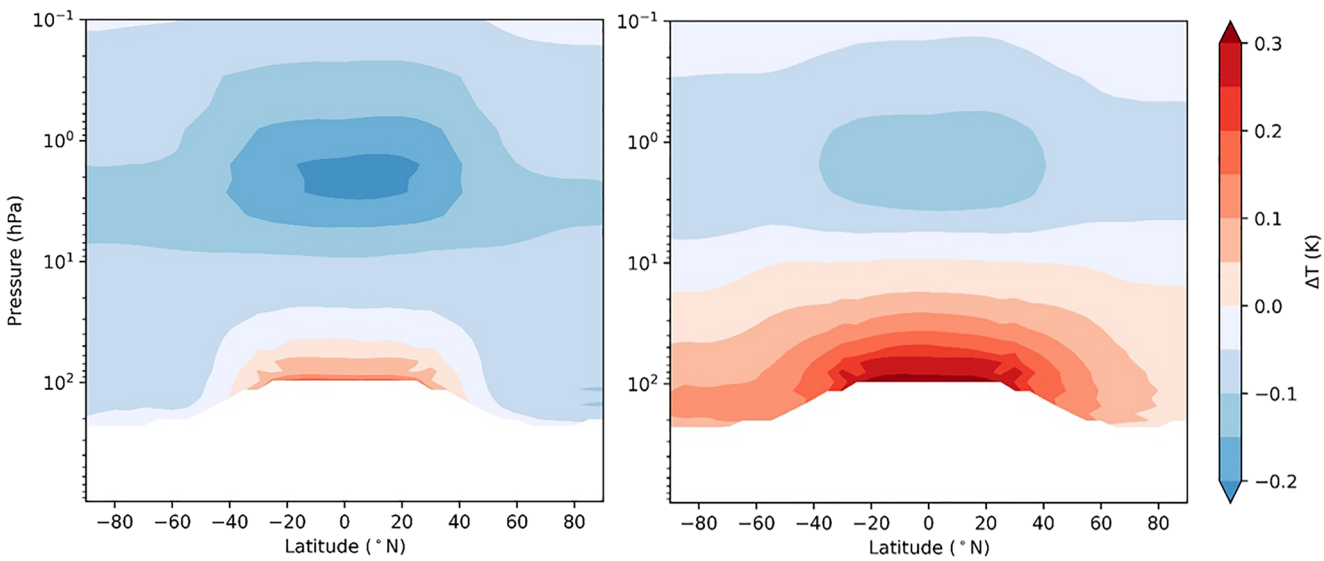

Figure 2. Annual zonal-mean ΔT (in K) following stratospheric temperature adjustment calculated using FDH for Longwave (LW)-only (left panel) and LW plus shortwave (SW) heating rates (right panel). Small oscillations in ΔT occur near the tropopause when SW heating rates are included; therefore data in the right plot have been smoothed. Derived using conditions stated in Table 1 note.

As a result, the LW IRF of 0.578 W m^{-2} (Table 1) is increased to a SARF value of 0.611 W m^{-2} (Table 2). This increases further to 0.613 W m^{-2} when the SW IRF is included.

The temperature change is consistent with the idealized experiments of Modak et al. (2018) in which SW absorption causes stratospheric warming of around 0.8 K, peaking at 100 hPa for a 10x increase in CH_4. The peak 0.5 K warming calculated here is equivalent to a warming trend of around 0.05 K $decade^{-1}$, if it occurred at a steady rate.

Figure 1 (upper right) presents the first spatially resolved calculation of the total CH_4 SW radiative effect (to our knowledge) including both direct all-sky tropopause SW IRF and the effect of SW absorption on stratospheric temperatures. The inclusion of SW absorption increases net SARF (Figure 1, lower right) predominantly across the entire globe, with the largest enhancement across northern Africa and the Arabian Peninsula, but also in regions with extensive low cloud, such as the southern oceans.

The total SW effect of 7% is smaller than the 15% reported by Etminan et al. (2016). The difference is largely explained by the substantial difference in the magnitude of the SW tropopause IRF (0.002 W m^{-2} compared to 0.03 W m^{-2}), but also by the magnitude of stratospheric temperature-adjustment. Etminan et al. (2016) find this process has a slightly more negative effect on CH_4 LW IRF, decreasing it by 2% from 0.516 W m^{-2} to 0.504 W m^{-2}. Considering the total SW effect is measured relative to adjusted LW-only SARF, this yields a larger percentage increase from their LW-only SARF (0.504 W m^{-2}) to their net SARF (0.582 W m^{-2}).

In addition to the sensitivities addressed in Section 3.2, the total CH_4 SW effect also depends on state variables (and their spatial and temporal variation) that affect CH_4 LW forcing and FDH adjustment, including temperature, humidity and clouds. Text S5 in Supporting Information S1 discusses uncertainties associated with the calculation of SW tropopause IRF and LW SARF. Using the root-sum-square method, a total uncertainty of ±12% is attributed to LW SARF and a total uncertainty of ±25% is tentatively attributed to SW tropopause IRF (see Table S2 in Supporting Information S1). Given the highly sensitive nature of CH_4 SW tropopause IRF, we believe that Etminan et al.,'s ±25% estimate of uncertainty was too low, hence despite the improved methodology here, we adopt the same overall uncertainty. In total, given that the CH_4 SW effect is about 6% of the net SARF, this yields a total uncertainty of around ±13% in net CH_4 SARF.

An alternative perspective on CH_4 SW RF can be gained by examining TOA forcings which is more analogous to ERF estimates derived from ESMs (Shine et al., 2022). For SARF, the net TOA and tropopause forcings are identical (Table 2) as is the total impact of the SW forcing (i.e., 7%). However, unlike the tropopause IRF, the SW TOA IRF is not a residual of changes in upward and downward irradiance and a more confident assessment is possible. TOA SW IRF is 0.082 W m^{-2} (or 13% of TOA net SARF). Stratospheric heating by SW absorption leads to an increase in TOA LW irradiance which drives a reduction in TOA LW SARF from 0.574 to 0.530 W m^{-2} (Table 2). Figure S9 in Supporting Information S1 shows the spatial distribution of annual-mean all-sky SW IRF (and corresponding CRE), total SW radiative effect and net SARF from a TOA perspective.

4. Discussion

Accurate quantification of CH_4 SW RF is dependent on spatially resolved specifications of CH_4 vertical profiles, CRE and spectrally resolved α_s to capture their collective heterogeneous effect on SW absorption. It is also dependent on inclusion of solar mid-infrared absorption. Further studies that incorporate these factors and explore other uncertainties (e.g., the representation of clouds and their overlap) are needed, particularly to constrain the sign and magnitude of clear-sky tropopause IRF and the size of CRE. Similarly, the SW RF of other gases could also be explored in detail.

Ongoing experiments as part of RFMIP (see Pincus et al., 2016) aim to expose radiative transfer parameterization error in ESM radiation schemes. Such analysis is essential to help quantify the accuracy of CH_4 SW absorption in particular; Text S5 in Supporting Information S1 presents evidence that CH_4 SW IRF is significantly underestimated in some such schemes.

The representation of radiative processes in ESMs is also important with respect to the calculation of individual adjustments. Adjustments for a tripling of CH_4 have been calculated by Smith et al. (2018) in 11 ESMs using radiative kernels and the RFMIP (Pincus et al., 2016) fixed-SST approach. Four of these ESMs included CH_4 SW

absorption bands. Although this is a small sample of models, the inclusion or omission of these bands appears to dictate the magnitude of H_2O adjustment and whether stratospheric temperature and cloud adjustments have a negative or positive effect on CH_4 forcing; this could only be confidently established if those models were run without these SW bands. Models that include CH_4 SW absorption simulate a negative stratospheric temperature adjustment to a CH_4 perturbation, consistent with the sign derived here from a TOA perspective. Although uncertainties are large in Smith et al. (2018), there is an indication that the total CH_4 adjustment is negative when SW absorption is included and positive when it is not.

IPCC AR6 (Forster et al., 2021) calculate CH_4 SARF using the simplified expression of Meinshausen et al. (2020) which incorporates the total CH_4 SW effect of 15% estimated by Etminan et al. (2016). The CH_4 ERF is estimated using the tropospheric adjustments of Smith et al. (2018) from the four ESMs that include CH_4 SW absorption. Overall, these adjustments reduce the ERF relative to TOA IRF by −14% (±15%; Forster et al., 2021). According to the total CH_4 SW effect of 7% presented here, IPCC AR6 CH_4 SARF and CH_4 ERF are both slightly overestimated. However, as stated above, the magnitude of tropospheric CH_4 adjustments are uncertain; further assessment is needed by ESMs that include validated treatment of CH_4 SW absorption.

5. Conclusions

Accurate quantification of CH_4 SW RF depends on realistic spatial and temporal representations of CH_4 vertical profiles, CRE, spectrally resolved α_s and inclusion of solar mid-infrared CH_4 absorption. At the surface, CH_4 SW IRF counteracts around 90% of CH_4 LW IRF resulting in a residual net IRF of 0.017 W m^{-2}. At the tropopause, CH_4 SW IRF is highly sensitive to the magnitude of the upward and downward forcing components and is significantly smaller than previous estimates at 0.002 W m^{-2} (±25%). However, the total CH_4 SW effect can only be fully quantified when the impact of stratospheric CH_4 SW absorption is included in the calculation of CH_4 SARF. Consequently, inclusion of SW absorption enhances the LW-only SARF by 0.039 W m^{-2} (i.e., by 7%) from 0.574 W m^{-2} to 0.613 W m^{-2} for a 750–1,800 ppb perturbation. An alternative TOA perspective demonstrates that the SW IRF of 0.082 W m^{-2} is 13% of TOA net SARF; the total effect of SW absorption is still 7% (i.e., in agreement with the tropopause view) as a result of stratospheric temperature adjustment. This indicates that the perception of the role of SW RF (particularly the direct impact of SW IRF and the impact of stratospheric temperature adjustment) depends on the perspective taken. In the ERF framework, the TOA view is becoming more prevalent.

Data Availability Statement

The SOCRATES radiative transfer code and documentation is available from https://code.metoffice.gov.uk/trac/socrates under an open source license but requires a free account from the UK Met Office (Scientific_Partnerships@metoffice.gov.uk) to access the website. ERA-interim renalysis, SCIAMACHY LER and MIPAS CH_4 climatology data are available via the in-text references Dee et al. (2011), Tilstra et al. (2017), and Hegglin et al. (2021), respectively. Datasets containing principal results (monthly means) are available at the University of Reading Research Data Archive via https://doi.org/10.17864/1947.000396 (Byrom & Shine, 2022).

Acknowledgments
REB thanks the NERC Scenario Doctoral Training Partnership for funding her PhD studentship (grant number NE/L002566/1). We thank William D. Collins (University of California, Berkeley) for valuable discussions in the early stages of this work. We also thank Bill Collins (University of Reading), Michaela Hegglin and Amanda Maycock for their input and Ramiro Checa-Garcia, Jonathan Elsey, and James Manners for their help in model development. Helpful reviewer comments also led to improvements.

References

Byrom, R. E., & Shine, K. P. (2022). Monthly-mean radiative forcings following an increase in methane from 750 ppb to 1800 ppb. *University of Reading Research Data Archive*. https://doi.org/10.17864/1947.000396

Checa-Garcia, R., Hegglin, M. I., Kinnison, D., Plummer, D. A., & Shine, K. P. (2018). Historical tropospheric and stratospheric ozone radiative forcing using the CMIP6 database. *Geophysical Research Letters*, *45*(7), 3264–3273. https://doi.org/10.1002/2017GL076770

Collins, W. D., Rasch, P. J., Boville, B. A., McCaa, J., Williamson, D. L., Kiehl, J. T., et al. (2004). *Description of the NCAR Community atmosphere model (CAM 3.0) (No*. NCAR/TN-464+STR). https://doi.org/10.5065/D63N21CH

Collins, W. D., Feldman, D. R., Kuo, C., & Nguyen, N. H. (2018). Large regional shortwave forcing by anthropogenic methane informed by Jovian observations. *Science Advances*, *4*(9), eaas9593. https://doi.org/10.1126/sciadv.aas9593

Cox, C., & Munk, W. (1954). Measurement of the roughness of the sea surface from photographs of the Sun's Glitter. *Journal of the Optical Society of America*, *44*(11), 838–850. https://doi.org/10.1364/JOSA.44.000838

Dee, D. P., Uppala, S. M., Simmons, A. J., Berrisford, P., Poli, P., Kobayashi, S., et al. (2011). The ERA-interim reanalysis: Configuration and performance of the data assimilation system. *Quarterly Journal of the Royal Meteorological Society*, *137*(656), 553–597. https://doi.org/10.1002/qj.828

Dudhia, A. (2017). The reference forward model (RFM). *Journal of Quantitative Spectroscopy and Radiative Transfer*, *186*, 243–253. https://doi.org/10.1016/j.jqsrt.2016.06.018

Edwards, J. M., & Slingo, A. (1996). Studies with a flexible new radiation code. I: Choosing a configuration for a large-scale model. *Quarterly Journal of the Royal Meteorological Society*, *122*(531), 689–719. https://doi.org/10.1002/qj.49712253107

Etminan, M., Myhre, G., Highwood, E. J., & Shine, K. P. (2016). Radiative forcing of carbon dioxide, methane, and nitrous oxide: A significant revision of the methane radiative forcing. *Geophysical Research Letters*, *43*(24), 614–623. https://doi.org/10.1002/2016GL071930

Fels, S. B., Mahlman, J. D., Schwarzkopf, M. D., & Sinclair, R. W. (1980). Stratospheric sensitivity to perturbations in ozone and carbon dioxide: Radiative and dynamical response. *Journal of the Atmospheric Sciences*, *37*(10), 2265–2297. https://doi.org/10.1175/1520-0469(1980)037<2265:sstpio>2.0.co;2

Forster, P., Storelvmo, T., Armour, K., Collins, W., Dufresne, J.-L., Frame, D., et al. (2021). The Earth's energy budget, climate feedbacks, and climate sensitivity. In *Climate change 2021: The physical science basis. Contribution of Working Group I to the Sixth Assessment Report of the Intergovernmental Panel on Climate Change*. https://doi.org/10.1017/9781009157896.009

Hansen, J., Sato, M., Ruedy, R., Nazarenko, L., Lacis, A., Schmidt, G. A., et al. (2005). Efficacy of climate forcings. *Journal of Geophysical Research*, *110*(D18). https://doi.org/10.1029/2005JD005776

Hegglin, M. I., Tegtmeier, S., Anderson, J., Bourassa, A. E., Brohede, S., Degenstein, D., et al. (2021). Overview and update of the SPARC data Initiative: Comparison of stratospheric composition measurements from satellite limb sounders. *Earth System Science Data*, *13*(5), 1855–1903. https://doi.org/10.5194/essd-13-1855-2021

Kleipool, Q. L., Dobber, M. R., De Haan, J. F., & Levelt, P. F. (2008). Earth surface reflectance climatology from 3 years of OMI data. *Journal of Geophysical Research*, *113*(D18). https://doi.org/10.1029/2008JD010290

Lean, J., Rottman, G., Harder, J., & Kopp, G. (2005). SORCE contributions to new understanding of global change and solar variability. *Solar Physics*, *230*(1), 27–53. https://doi.org/10.1007/s11207-005-1527-2

Li, J., Curry, C. L., Sun, Z., & Zhang, F. (2010). Overlap of solar and infrared spectra and the shortwave radiative effect of methane. *Journal of the Atmospheric Sciences*, *67*(7), 2372–2389. https://doi.org/10.1175/2010JAS3282.1

Manners, J., Edwards, J. M., Hill, P., & Thelen, J.-C. (2015). *SOCRATES (Suite Of Community RAdiative Transfer codes based on Edwards and Slingo)* Technical Guide, Met Office. (Access requires a free account from the UK Met Office: Scientific_Partnerships@metoffice.gov.uk) Retrieved from https://code.metoffice.gov.uk/trac/socrates

Meinshausen, M., Nicholls, Z. R. J., Lewis, J., Gidden, M. J., Vogel, E., Freund, M., et al. (2020). The shared socio-economic pathway (SSP) greenhouse gas concentrations and their extensions to 2500. *Geoscientific Model Development*, *13*(8), 3571–3605. https://doi.org/10.5194/gmd-13-3571-2020

Mlawer, E. J., Payne, V. H., Moncet, J.-L., Delamere, J. S., Alvarado, M. J., & Tobin, D. C. (2012). Development and recent evaluation of the MT_CKD model of continuum absorption. *Philosophical Transactions of the Royal Society A: Mathematical, Physical & Engineering Sciences*, *370*(1968), 2520–2556. https://doi.org/10.1098/rsta.2011.0295

Modak, A., Bala, G., Caldeira, K., & Cao, L. (2018). Does shortwave absorption by methane influence its effectiveness? *Climate Dynamics*, *51*(9), 3653–3672. https://doi.org/10.1007/s00382-018-4102-x

Myhre, G., Samset, B. H., Schulz, M., Balkanski, Y., Bauer, S., Berntsen, T. K., et al. (2013). Radiative forcing of the direct aerosol effect from AeroCom Phase II simulations. *Atmospheric Chemistry and Physics*, *13*(4), 1853–1877. https://doi.org/10.5194/acp-13-1853-2013

Myhre, G., Shindell, D., Bréon, F.-M., Collins, W., Fuglestvedt, J., Huang, J., et al. (2013). Anthropogenic and natural radiative forcing. In *Climate change 2013: The physical science basis. Contribution of Working Group I to the Fifth Assessment Report of the Intergovernmental Panel on Climate Change*. C. U. Press. Retrieved from https://www.ipcc.ch/site/assets/uploads/2018/02/WG1AR5_Chapter08_FINAL.pdf

Myhre, G., Stordal, F., Gausemel, I., Nielsen, C. J., & Mahieu, E. (2006). Line-by-line calculations of thermal infrared radiation representative for global condition: CFC-12 as an example. *Journal of Quantitative Spectroscopy and Radiative Transfer*, *97*(3), 317–331. https://doi.org/10.1016/j.jqsrt.2005.04.015

Pincus, R., Forster, P. M., & Stevens, B. (2016). The radiative forcing model intercomparison project (RFMIP): Experimental protocol for CMIP6. *Geoscientific Model Development*, *9*(9), 3447–3460. https://doi.org/10.5194/gmd-9-3447-2016

Ptashnik, I. V., McPheat, R. A., Shine, K. P., Smith, K. M., & Williams, R. G. (2011). Water vapor self-continuum absorption in near-infrared windows derived from laboratory measurements. *Journal of Geophysical Research*, *116*(D16). https://doi.org/10.1029/2011JD015603

Ptashnik, I. V., McPheat, R. A., Shine, K. P., Smith, K. M., & Williams, R. G. (2012). Water vapour foreign-continuum absorption in near-infrared windows from laboratory measurements. *Philosophical Transactions of the Royal Society A: Mathematical, Physical & Engineering Sciences*, *370*(1968), 2557–2577. https://doi.org/10.1098/rsta.2011.0218

Ramaswamy, V., Collins, W., Haywood, J., Lean, J., Mahowald, N., Myhre, G., et al. (2019). Radiative forcing of climate: The historical evolution of the radiative forcing concept, the forcing agents and their quantification, and applications. *Meteorological Monographs*, *59*, 14.11–14.101. https://doi.org/10.1175/amsmonographs-d-19-0001.1

Rothman, L. S., Gordon, I. E., Babikov, Y., Barbe, A., Chris Benner, D., Bernath, P. F., et al. (2013). The HITRAN2012 molecular spectroscopic database. *Journal of Quantitative Spectroscopy and Radiative Transfer*, *130*, 4–50. https://doi.org/10.1016/j.jqsrt.2013.07.002

Shine, K. P., Byrom, R. E., & Checa-Garcia, R. (2022). Conceptual understanding of shortwave radiative forcing by greenhouse gases. *Atmospheric Science Letters*, e1116. https://doi.org/10.1002/asl.1116

Smith, C. J., Kramer, R. J., Myhre, G., Forster, P. M., Soden, B. J., Andrews, T., et al. (2018). Understanding rapid adjustments to diverse forcing agents. *Geophysical Research Letters*, *45*(21), 12023–12031. https://doi.org/10.1029/2018GL079826

Tilstra, L. G., Tuinder, O. N. E., Wang, P., & Stammes, P. (2017). Surface reflectivity climatologies from UV to NIR determined from Earth observations by GOME-2 and SCIAMACHY. *Journal of Geophysical Research: Atmospheres*, *122*(7), 4084–4111. https://doi.org/10.1002/2016JD025940

Walters, D., Baran, A. J., Boutle, I., Brooks, M., Earnshaw, P., Edwards, J., et al. (2019). The Met Office unified model global atmosphere 7.0/7.1 and JULES global land 7.0 configurations. *Geoscientific Model Development*, *12*(5), 1909–1963. https://doi.org/10.5194/gmd-12-1909-2019

References From the Supporting Information

Anisman, L. O., Chubb, K. L., Elsey, J., Al-Refaie, A., Changeat, Q., Yurchenko, S. N., et al. (2022). Cross-sections for heavy atmospheres: H2O continuum. *Journal of Quantitative Spectroscopy and Radiative Transfer*, *278*, 108013. https://doi.org/10.1016/j.jqsrt.2021.108013

Briegleb, B., & Ramanathan, V. (1982). Spectral and Diurnal Variations in Clear Sky Planetary Albedo. *Journal of Applied Meteorology (1962-1982)*, *21*(8), 1160–1171. https://doi.org/10.1175/1520-0450(1982)021%3C1160:SADVIC%3E2.0.CO;2

Checa-Garcia, R., Hegglin, M. I., Kinnison, D., Plummer, D. A., & Shine, K. P. (2018). Historical Tropospheric and Stratospheric Ozone Radiative Forcing Using the CMIP6 Database. *Geophysical Research Letters*, *45*(7), 3264–3273. https://doi.org/10.1002/2017GL076770

Choi, W. K., & Holton, J. R. (1991). Transport of N_2O in the stratosphere related to the equatorial semiannual oscillation. *Journal of Geophysical Research: Atmospheres*, *96*(D12), 22543–22557. https://doi.org/10.1029/91JD02263

Errera, Q., Ceccherini, S., Christophe, Y., Chabrillat, S., Hegglin, M. I., Lambert, A., et al. (2016). Harmonisation and diagnostics of MIPAS ESA CH_4 and N_2O profiles using data assimilation. *Atmospheric Measurement Techniques*, *9*(12), 5895–5909. https://doi.org/10.5194/amt-9-5895-2016

Freckleton, R. S., Highwood, E. J., Shine, K. P., Wild, O., Law, K. S., & Sanderson, M. G. (1998). Greenhouse gas radiative forcing: Effects of averaging and inhomogeneities in trace gas distribution. *Quarterly Journal of the Royal Meteorological Society*, *124*(550), 2099–2127. https://doi.org/10.1002/qj.49712455014

Hale, G. M., & Querry, M. R. (1973). Optical Constants of Water in the 200-nm to 200-μm Wavelength Region. *Applied Optics*, *12*(3), 555–563. https://doi.org/10.1364/AO.12.000555

Hodnebrog, Ø., Etminan, M., Fuglestvedt, J. S., Marston, G., Myhre, G., Nielsen, C. J., et al. (2013). Global warming potentials and radiative efficiencies of halocarbons and related compounds: A comprehensive review. *Reviews of Geophysics*, *51*(2), 300–378. https://doi.org/10.1002/rog.20013

Hodnebrog, Ø., Myhre, G., Kramer, R. J., Shine, K. P., Andrews, T., Faluvegi, G., et al. (2020). The effect of rapid adjustments to halocarbons and N_2O on radiative forcing. *NPJ Climate and Atmospheric Science*, *3*(1), 43. https://doi.org/10.1038/s41612-020-00150-x

Hogan, R. J., & Matricardi, M. (2020). Evaluating and improving the treatment of gases in radiation schemes: The correlated K-distribution model intercomparison project (CKDMIP). *Geoscientific Model Development*, *13*(12), 6501–6521. https://doi.org/10.5194/gmd-13-6501-2020

Huang, X., Chen, X., Flanner, M., Yang, P., Feldman, D., & Kuo, C. (2018). Improved Representation of Surface Spectral Emissivity in a Global Climate Model and Its Impact on Simulated Climate. *Journal of Climate*, *31*(9), 3711–3727. https://doi.org/10.1175/jcli-d-17-0125.1

IFS Documentation CY47R1. (2020). Part IV: Physical Processes. In *IFS Documentation CY47R1*. ECMWF. Retrieved from https://www.ecmwf.int/node/19748

Jerlov, N. G. (1976). *Marine optics* (2 ed.). Elsevier Scientific Pub. Co. (ISBN: 9780080870502).

Laeng, A., Plieninger, J., Von Clarmann, T., Grabowski, U., Stiller, G., Eckert, E., et al. (2015). Validation of MIPAS IMK/IAA methane profiles. *Atmospheric Measurement Techniques*, *8*(12), 5251–5261. https://doi.org/10.5194/amt-8-5251-2015

Oreopoulos, L., Mlawer, E., Delamere, J., Shippert, T., Cole, J., Fomin, B., et al. (2012). The Continual Intercomparison of Radiation Codes: Results from Phase I. *Journal of Geophysical Research: Atmospheres*, *117*(D6). https://doi.org/10.1029/2011JD016821

Pincus, R., Mlawer, E. J., Oreopoulos, L., Ackerman, A. S., Baek, S., Brath, M., et al. (2015). Radiative flux and forcing parameterization error in aerosol-free clear skies. *Geophysical Research Letters*, *42*(13), 5485–5492. https://doi.org/10.1002/2015GL064291

Plieninger, J., Laeng, A., Lossow, S., Von Clarmann, T., Stiller, G. P., Kellmann, S., et al. (2016). Validation of revised methane and nitrous oxide profiles from MIPAS–ENVISAT. *Atmospheric Measurement Techniques*, *9*(2), 765–779. https://doi.org/10.5194/amt-9-765-2016

Ricaud, P., Sič, B., Elamraoui, L., Attié, J. L., Zbinden, R., Huszar, P., et al. (2014). Impact of the Asian monsoon anticyclone on the variability of mid-to-upper tropospheric methane above the Mediterranean Basin. *Atmospheric Chemistry and Physics*, *14*(20), 11427–11446. https://doi.org/10.5194/acp-14-11427-2014

Roesch, A., Wild, M., Pinker, R., & Ohmura, A. (2002). Comparison of spectral surface albedos and their impact on the general circulation model simulated surface climate. *Journal of Geophysical Research: Atmospheres*, *107*(D14), ACL13-11–ACL13-18. https://doi.org/10.1029/2001JD000809

Séférian, R., Baek, S., Boucher, O., Dufresne, J. L., Decharme, B., Saint-Martin, D., & Roehrig, R. (2018). An interactive ocean surface albedo scheme (OSAv1.0): Formulation and evaluation in ARPEGE-Climat (V6.1) and LMDZ (V5A). *Geoscientific Model Development*, *11*(1), 321–338. https://doi.org/10.5194/gmd-11-321-2018

SPARC. (2017). The SPARC Data Initiative: Assessment of stratospheric trace gas and aerosol climatologies from satellite limb sounders SPARC Report No. 8. WCRP-5/2017, Issue. Retrieved from www.sparc-climate.org/publications/sparc%20reports/sparc-report-no-8/

Von Clarmann, T., Höpfner, M., Kellmann, S., Linden, A., Chauhan, S., Funke, B., et al. (2009). Retrieval of temperature, H_2O, O_3, HNO_3, CH_4, N_2O, $ClONO_2$ and ClO from MIPAS reduced resolution nominal mode limb emission measurements. *Atmospheric Measurement Technique*, *2*(1), 159–175. https://doi.org/10.5194/amt-2-159-2009

Whitlock, C. H., Bartlett, D. S., & Gurganus, E. A. (1982). Sea foam reflectance and influence on optimum wavelength for remote sensing of ocean aerosols. *Geophysical Research Letters*, *9*(6), 719–722. https://doi.org/10.1029/GL009i006p00719

Xiong, X., Houweling, S., Wei, J., Maddy, E., Sun, F., & Barnet, C. (2009). Methane plume over south Asia during the monsoon season: Satellite observation and model simulation. *Atmospheric Chemistry and Physics*, *9*(3), 783–794. https://doi.org/10.5194/acp-9-783-2009